

# Coherence and feedback in supersonic rectangular jet screech

By G. J. Wu, S. K. Lele AND J. Jeun

## 1. Motivation and objectives

Screech is an aeroacoustic resonance phenomenon in nonperfectly expanded supersonic jets first discovered by Powell (1953). Screech produces high-intensity tones at distinct frequencies, making it a notoriously riling component of supersonic jet noise. In addition, jet screech can induce high dynamic loading, which, if it is close to the structural resonance frequencies, could cause premature fatigue failures of components around the jet engines such as those reported on VC10, F-15, B1-B, and F-35 (Raman 1997; Raman *et al.* 2012; Majumdar 2014).

Previous research on supersonic jet screech has been comprehensively reviewed by Raman (1999) and Edgington-Mitchell (2019), who highlight the experimental observations from the 1950s to date and the theories based on these empirical findings. The classical description of screech contains four components: the downstream-traveling instability waves originated from the jet initial shear layer, the interactions between instability waves and shock cells in the jet plume, the upstream-traveling component that re-excites the initial shear layer, and the receptivity process of the shear layer near the nozzle exit at selective frequencies.

On the basis of certain phase criteria for the closed feedback loop, it is possible to derive a semi-empirical formula that can accurately predict the screech frequencies. However, to this date no simple models exist for predicting screech amplitude, due to the lack of a clear systematic understanding of the individual processes. The downstream-traveling component is the Kelvin-Helmholtz (K-H) instability wave and it provides energy to the screech loop (Tam & Ahuja 1990). The upstream-traveling component is less well understood. Powell's original depiction of screech considers upstream-traveling acoustic waves outside the jet plume to be the closure mechanism. On the other hand, Tam & Hu (1989) discovered an internal upstream-propagating acoustic mode inside the jet plume, and various experimental and numerical evidence suggests this internal acoustic mode can also participate in screech closure (Gojon *et al.* 2016; Bogey & Gojon 2017; Edgington-Mitchell *et al.* 2018; Gojon *et al.* 2019). The interactions between downstream-traveling instability waves and oscillating shock cells release acoustic radiation over a range of frequencies, including the broadband shock associated noise (BBSAN) and the tonal components of screech, and the directivity patterns for the screech fundamental tone and its harmonic tones vary significantly. The fundamental tone dominates in the upstream and downstream directions and the first harmonic is strongest at the sideline angle. To explain these directivity patterns, Powell (1953) derived a source model consisting of three or four simple sources at the same frequency separated by the average shock cell spacing along the jet axis. An alternative model by Tam *et al.* (1986) formulates screech as a special case of BBSAN from spatially distributed sources caused by interactions between instability waves and shock cells.

The current work uses high-fidelity large-eddy simulations (LES) data to analyze the

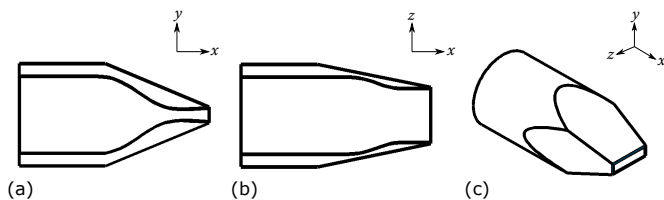


FIGURE 1. Nozzle geometry. (a) Minor-axis ( $x$ - $y$ ) plane, (b) major-axis ( $x$ - $z$ ) plane, (c) external view.

dominant coherence involved in the screech feedback loop and intends to improve the current understanding of screech generation in a rectangular jet. Through previous works, the numerical results have been validated against experiments conducted at Florida State University. Excellent agreement between the LES data and the experimental data is found (Wu *et al.* 2020a,b) and is briefly highlighted in this report in terms of velocity profiles and near- and far-field acoustics. Using the LES data, the dominant coherent structures at the screech fundamental and first harmonic frequencies are examined. At the fundamental frequency, there exist both external and internal upstream-traveling waves, and their strength and phase velocities are estimated together with the downstream-traveling K-H waves. Lastly, the two possible feedback paths for screech closure are assessed in terms of resonance phase criteria using spectral proper orthogonal decomposition (SPOD) (Lumley 1970; Towne *et al.* 2018; Schmidt & Colonius 2020).

## 2. Nozzle geometry and flow parameters

The rectangular nozzle was designed by Florida State University for experimental studies of screech by Alkislar *et al.* (2003) and Valentich *et al.* (2016). As shown in Figure 1, the convergent section is designed using a 5th-order polynomial, and the divergent section in the minor-axis plane is designed by the method of characteristics for an ideal expansion at Mach 1.44. In the major-axis plane, the nozzle surfaces are kept straight downstream of the throat. Starting from a circular cross section of 57.15 mm in diameter, the nozzle smoothly transitions to a rectangular shape at the exit with a 4:1 aspect ratio. The minor dimension of the exit  $h$  is 10 mm, and the major dimension  $w$  is 40 mm. The equivalent jet diameter,  $D_e = 2\sqrt{hw/\pi}$ , is 22.6 mm. In the remainder of this work,  $+x$  is used to denote the jet streamwise direction,  $y$  is in the minor-axis direction,  $z$  is in the major-axis direction, and  $\phi$  is the jet polar angle measured with respect to the jet centerline starting from the upstream direction. LES results computed from a mesh containing 140 million grids at three underexpanded screech conditions with  $M_j = 1.56, 1.69, 1.78$  are used in the analysis, where  $M_j$  is the fully expanded jet Mach number if under isentropic expansion. The flow parameters are summarized in Table 1.

## 3. Numerical setup

The LES are performed using the unstructured compressible flow solver CharLES (Brès *et al.* 2017), developed at Cascade Technologies, in concert with a Voronoi-based mesh generation paradigm (Brès *et al.* 2018, 2019). CharLES uses a shock-capturing method based on kinetic energy and entropy preserving (KEEP) schemes (Tadmor 2003; Chandrashekar 2013; Fisher & Carpenter 2013). The far-field noise of the jet is computed using an efficient permeable formulation (Lockard 2000) of the Ffowcs Williams–Hawkings

$p_{0t}/p_\infty$	$T_{0t}/T_\infty$	$M_j$	Simulation time ( $\Delta\tilde{t}$ )	Mesh size (million)
4.02	1	1.56	1400	
4.86	1	1.69	1500	140
5.57	1	1.78	700	

TABLE 1. Summary of flow parameters.  $p_{0t}$  and  $T_{0t}$  are the reservoir stagnation pressure and temperature,  $p_\infty$  and  $T_\infty$  are the static pressure and temperature in the ambient.  $\Delta\tilde{t} = \Delta t c_\infty/h$  is the normalized acoustic time unit based on nozzle minor dimension  $h$  and ambient speed of sound  $c_\infty$ .

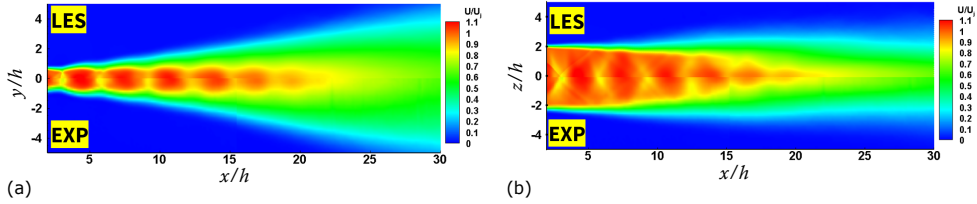


FIGURE 2. Comparison between LES and particle image velocimetry data of mean streamwise velocity in the (a) minor-axis plane and (b) major-axis plane. Screech case:  $M_j = 1.69$ .

(FW-H) equation (Ffowcs-Williams & Hawkings 1969) in the frequency domain discussed in detail in Brès *et al.* (2017). The grid and FW-H surface choices for the screech simulations have been discussed and assessed in Wu *et al.* (2020b).

## 4. Results and discussion

### 4.1. Comparison with experiment

LES data for the case at  $M_j = 1.69$  from the 140 million mesh over 1500 acoustic time units ( $\Delta\tilde{t} = \Delta t c/h$ ) are compared with experimental data and presented here. For more detailed data validation with experiment, see Wu *et al.* (2020b). Figure 2 shows the time-averaged streamwise velocity contours in the jet minor- and major-axis planes, with LES results plotted on the top half and experimental data plotted on the bottom half. In both planes the LES are able to accurately capture the mean shock cell structures and overall jet spreading. Figure 3 shows the far-field acoustic comparison between LES and experiments around  $270h$  away from the nozzle exit. The numerical results agree very well with microphone measurements in both the broadband noise spectra and the individual screech tones. The screech fundamental frequency expressed in  $St = fD_e/U_j$  is 0.23 for both LES and experiment.

### 4.2. Dominant coherent structures

With the SPOD method, the spatial-temporal coherent structures at screech frequencies can be extracted from the near-field flow data. The SPOD modes presented here are the eigenvectors of the cross-spectral density tensor formulated in the form of variance in pressure or velocity fluctuations over the area bounded by  $x/h \in [0, 150]$  and  $y/h \in [-20, 20]$  in the minor-axis plane. The SPOD modes form an orthogonal basis in space and time, with ranked eigenvalues representing the contribution of each mode to the total

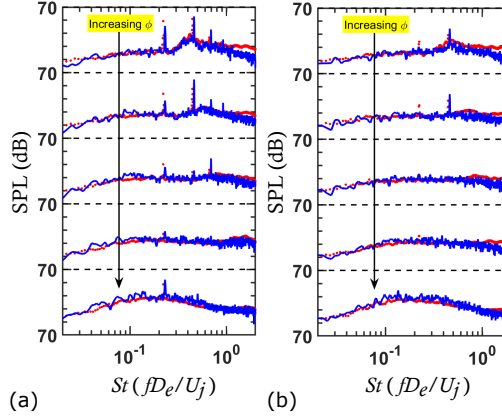


FIGURE 3. Comparison between LES (line) and experimental data (dot) of far-field acoustics in the (a) minor-axis plane and (b) major-axis plane. Screech case:  $M_j = 1.69$ . Spectra are stacked in the order of increasing  $\phi$  (deg) from top to bottom: 83, 103, 113, 123, 134, with each value rounded to the closest integer.

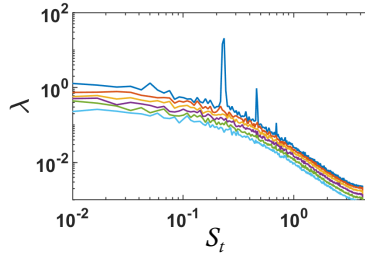


FIGURE 4. Energy spectra  $\lambda$  of the ranked SPOD modes calculated with  $p'$ . Each line is for one specific SPOD mode in space and frequency domain; here the energy spectra of the first six SPOD modes are shown.

variance of the near-field data. In the literature, the eigenvalues are also referred to as the energy spectra of the SPOD modes (Schmidt *et al.* 2018). Here, SPOD analysis is used to interrogate the leading coherent structures responsible for screech generation.

In this section, all the SPOD analysis presented is computed using data for the case at  $M_j = 1.69$  from a 140 million mesh. Using the pressure fluctuation  $p'$  over  $700 \Delta \tilde{t}$ , the leading-order SPOD modes are calculated and the energy spectra are shown in Figure 4. High-energy peaks are seen in the first mode at the screech frequencies. At the screech fundamental frequency, Figure 5 shows the first SPOD mode computed using pressure  $p'$  and  $v'$ , the velocity fluctuation in the minor-axis direction. At the fundamental frequency,  $St = 0.23$ , the first SPOD mode indicates the presence of spatially modulating standing wave patterns in the jet plume and their amplitudes peak between  $x/h = 10$  and  $x/h = 20$ . Similar standing wave structures have been observed and studied in detail in previous screech experiments (Panda 1999) and are formed as a result of the partial interference between oppositely traveling hydrodynamic and acoustic waves. The SPOD mode of  $p'$  is antisymmetric while that of  $v'$  is symmetric with respect to the jet axis.

At the first harmonic frequency, shapes of the first SPOD mode of  $p'$ ,  $u'$ , and  $v'$  are shown in Figure 6. The coherent structures exhibit a more complex pattern than those

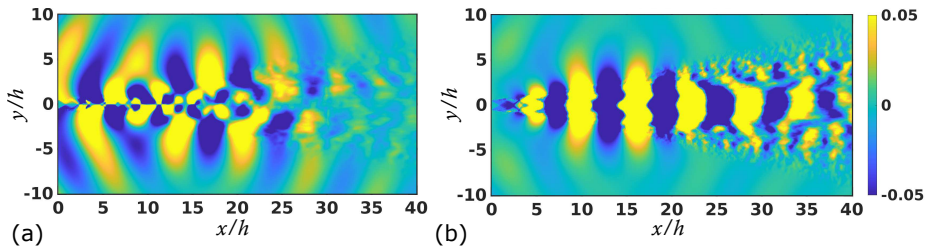


FIGURE 5. Shapes of the first SPOD mode at the screech fundamental frequency: (a)  $p'$  pressure fluctuation and (b)  $v'$  velocity fluctuation in the  $y$  direction. Values plotted are the real part of the SPOD shape function at the indicated phase normalized by its maximum modulus.

of the fundamental. A particularly noticeable feature in the  $p'$  SPOD mode shown in Figure 6(a) is the beaming of waves with a relatively flat wave front to the ambient at about 90 deg between  $x/h = 12$  and  $x/h = 21$ . This radiation seems to be associated with large-scale coherent structures inside the jet plume, as shown in a close-up view in Figure 6(d). Comparing the  $p'$  SPOD mode with those of  $u'$  and  $v'$  at the same phase in Figure 6(b,c), the large-scale structures are oblique and elongated in shape. They mostly appear in the irrotational region inside the jet and their length scale is larger than that of the coherent instability structures along the shear layer. The close-up views in Figure 6(e,f) show that when these oblique elongated structures come close to the jet shear layer, emission of sound outside the jet is observed. Coincidentally, the identified region of peak emission between  $x/h = 12$  and  $x/h = 21$  is near the end of the jet supersonic core, where intense shock fluctuations and jet flapping usually take place during screech. Correlating observations from these SPOD modes with the shock oscillation and jet flapping dynamics could help explain the sound generation mechanism for screech at the first harmonic frequency. This is planned in the future.

As seen in the  $p'$  SPOD modes from Figures 5(a) and 6(a), along with the acoustic pressure field shown in Figure 7, the screech fundamental and first harmonic tones display distinct directivity patterns. At the fundamental, acoustic waves are dominant in a limited range of upstream and downstream directions; at the first harmonic, the acoustic waves display a multiband pattern: one narrow band of polar angles around 90 deg with peak intensity and two weaker bands in the upstream and downstream directions. These multiband patterns are a consequence of interference among spatially distributed phased sources, which have been previously modeled either as an array of discrete point sources (Powell 1953) or as continuous sources (Tam *et al.* 1986). As a first-order approximation, one can determine an effective source location by back tracing the acoustic waves, and for the current case, the effective source location for the fundamental tone is found to be around  $x/h = 13.1$  (see Section 4.3 for details). Measured with respect to the effective source location, the directivity of the screech tones at  $r/h = 20$  is plotted in Figure 8.

#### 4.3. Feedback path investigation

To investigate the upstream-traveling waves involved in screech closure, the standing wave structure obtained by SPOD is further decomposed into upstream-traveling and downstream-traveling components, using the phase velocity direction, based on the sign of the spatial wavenumber in  $x$ , as a proxy for the direction of wave propagation. Figure 9 shows the isolated wave components from the first SPOD mode at  $St = 0.23$ . The downstream-traveling waves in Figure 9(b,d) are the K-H instability waves com-

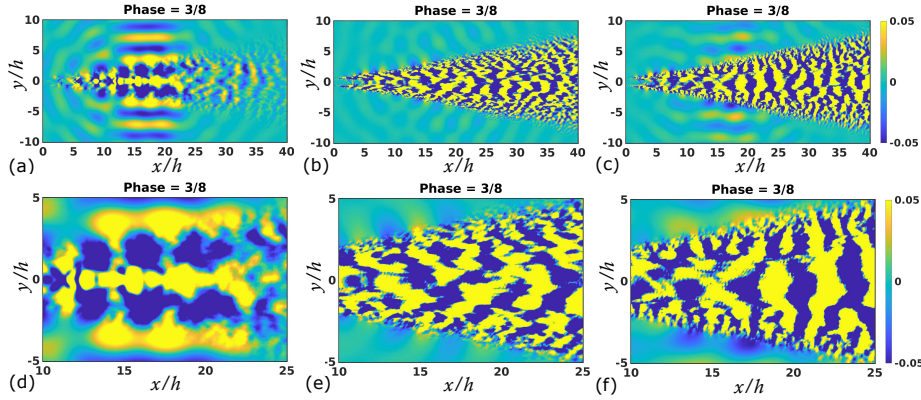


FIGURE 6. Shapes of the first SPOD modes at the first harmonic frequency of (a)  $p'$ , (b)  $u'$ , and (c)  $v'$ . Plots (d–f) are zoomed-in views of plots (a–c). Values plotted are the real part of the SPOD shape function at the indicated phase normalized by its maximum modulus.

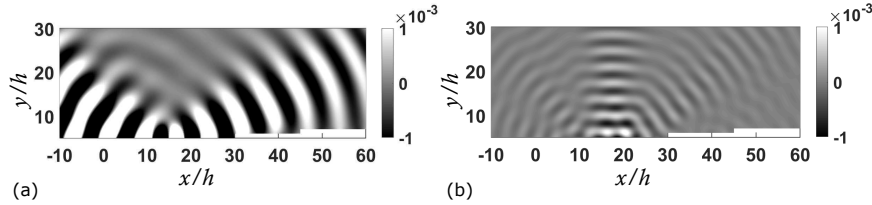


FIGURE 7. Instantaneous snapshot of  $p''/p_\infty$  at the screech fundamental, where  $p''$  is the acoustic pressure fluctuation calculated by the FW-H method and  $p_\infty$  is the ambient static pressure, Fourier filtered in time at (a) the screech fundamental frequency and (b) the first harmonic frequency. Screech case:  $M_j = 1.69$ .

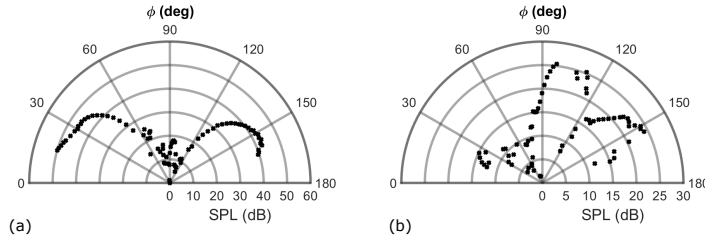


FIGURE 8. Screech tone directivity measured at  $r/h = 20$  with respect to  $(x/h, y/h) = (13.1, 0)$  in the jet minor-axis ( $x-y$ ) plane. (a) The screech fundamental tone and (b) the first harmonic tone.

only seen in high-speed subsonic and supersonic jets (Schmidt *et al.* 2018; Nekkanti & Schmidt 2020). In Figure 9(a,c) the upstream-traveling waves contain both an internal mode (Tam & Hu 1989) and external acoustic waves. The internal component has a peak region between  $x/h = 13$  and  $x/h = 20$  and decays rapidly upstream, reaching a similar amplitude as that of the external acoustic waves at the nozzle exit. To facilitate the remainder of the discussion, we use  $k_-$  to denote the upstream-propagating internal mode and  $k_+$  to denote the downstream-propagating K-H wave.

Using the SPOD data, the phase velocity and the variation in amplitude of each wave component can be inferred from cross-correlating signals between the nozzle exit and

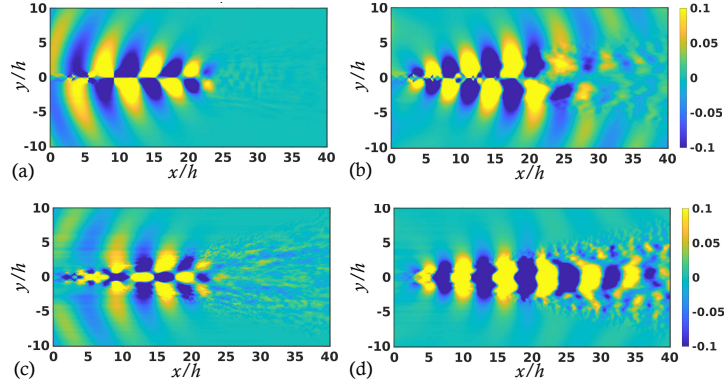


FIGURE 9. (Left) Upstream-traveling and (right) downstream-traveling wave components from the first SPOD modes at the screech fundamental frequency. (a,b)  $p'$  and (c,d)  $v'$ . Screech case:  $M_j = 1.69$ .

various downstream locations at a fixed height above the jet centerline. If a traveling wave is detected by two probes at different streamwise locations, the signals are related as

$$q(x_2, y_c, t) = \alpha q(x_1, y_c, t - \tau) + n(t), \quad (4.1)$$

where  $q(x_i, y_c, t)$  is a zero-mean stationary signal of any flow variable at a particular streamwise location  $x_i$  along the line  $y = y_c$ ,  $\alpha$  is the coefficient of growth or decay in wave amplitude,  $\tau$  is the time delay accounting for the traveling time from one location to another, and  $n(t)$  is the random noise with a zero mean. The cross-correlation function between the stationary signals is

$$\begin{aligned} R_{12}(\tau') &= E [q(x_1, t)q(x_2, t + \tau')] \\ &= E [q(x_1, t) (\alpha q(x_1, t + \tau' - \tau) + n(t))] \\ &= \alpha R_{11}(\tau' - \tau), \end{aligned} \quad (4.2)$$

where the autocorrelation function is

$$R_{11}(\tau') = E [q(x_1, t)q(x_1, t + \tau')]. \quad (4.3)$$

Using the Wiener-Khinchin relations, the cross-correlation function can be calculated (if the unbounded integral exists) by

$$R_{12}(\tau') = \int_{-\infty}^{\infty} S_{12}(f) e^{i2\pi f\tau'} df. \quad (4.4)$$

$S_{12}$  is the cross-spectral density function between  $q(x_1, y_c, t)$  and  $q(x_2, y_c, t)$  defined as

$$S_{12}(f) = \lim_{T \rightarrow \infty} \frac{1}{T} E [\hat{q}^{*(n)}(x_1, y_c, f) \hat{q}^{(n)}(x_2, y_c, f)], \quad (4.5)$$

where  $\hat{q}^{(n)}$  are the finite Fourier transforms of the signal  $q^{(n)}(t)$  from the  $n$ th realization of data sampling, and  $T$  is the length in time interval of each realization. Since signals from the SPOD mode at each frequency are harmonic functions in time, the cross-spectral density function at the screech fundamental frequency is simply

$$S_{12}(f) = \begin{cases} 0 & \text{if } f \neq f_{sc} \\ \frac{1}{T} \hat{q}^*(x_1, y_c, f_{sc}) \hat{q}(x_2, y_c, f_{sc}) & \text{otherwise,} \end{cases} \quad (4.6)$$

where  $f_{sc}$  is the screech fundamental frequency. The finite record estimate of the correlation function becomes

$$R_{12}(\tau') \approx \hat{q}_1^*(f_{sc})\hat{q}_2(f_{sc})e^{i2\pi f_{sc}\tau'}, \quad (4.7)$$

$$R_{11}(\tau' - \tau) \approx \hat{q}_1^*(f_{sc})\hat{q}_1(f_{sc})e^{i2\pi f_{sc}(\tau' - \tau)}. \quad (4.8)$$

By substituting Eqs. (4.7)-(4.8) to Eq. (4.2) and solving for  $\tau$  and  $\alpha$ , we get

$$\tau = \frac{\arg\zeta}{-i2\pi f_{sc}}, \quad \alpha = |\zeta|, \quad \zeta = \frac{\hat{q}_1^*\hat{q}_2}{\hat{q}_1^*\hat{q}_1}. \quad (4.9)$$

Using Eq. (4.9), the time delay  $\tau$  between signals is computed using the first SPOD mode of  $p'$  along the line  $y/h = 6$  and the reference location is at  $x/h = 0$ . Seen in Figure 10(a), this line traces the external acoustic waves. As the streamwise location varies, the normalized time delay  $\tau/T_{sc}$  of a downstream signal with respect to the reference at  $x/h = 0$  is shown in Figure 10(d), where  $T_{sc}$  is the screech period. The sign switch of the slope clearly reveals both external upstream-propagating and downstream-propagating acoustic waves. These waves originate from a distributed source region, bounded by  $x/h \approx 11$  and 15. In a first-order estimate, one could use an effective source location,  $x_s$ . Additionally, by performing least square linear fits to the two segments of the time delay variation, the streamwise phase velocity of the external acoustic waves, denoted by  $U_{c-}$  and  $U_{c+}$  for upstream- and downstream-propagating waves, can be calculated. Based on the ratio of  $U_{c\pm}/c_\infty$ , the angle of the acoustic radiation,  $\beta_\pm$ , measured from  $x_s$  with respect to the jet axis can also be approximated. These results are reported in Table 2 for the three jet screech cases considered. As  $M_j$  increases, the location of the effective source for the external acoustic waves move farther downstream. In addition, the downstream radiation moves farther away from the jet axis with increasing  $M_j$ , but the upstream radiation angle does not indicate a clear trend for the three cases considered.

Considering the instability waves inside the jet plume, the first SPOD mode of  $v'$  at the screech fundamental frequency is used. The data are first decomposed to contain only the upstream- or downstream-propagating component, and cross correlation is computed along the nozzle lip line  $y/h = 0.5$  with a reference probe at  $x/h = 0$ . Figure 10(b,c) highlights the locations being considered with respect to the SPOD structures. Figure 10(e,f) suggests the time delays of the  $k_-$  and  $k_+$  waves vary almost linearly with respect to the streamwise distance in the region between  $x/h = 10$  and  $x/h = 25$ . The streamwise phase velocities of the  $k_-$  and  $k_+$  waves can be approximated using linear least square fitting. The results are summarized in Table 2 and denoted as  $U_{k+}$  and  $U_{k-}$ . When scaled by the ideally expanded jet velocity  $U_j$ , all three screech cases report very similar values for the convective velocities, with  $U_{k+}/U_j$  slightly larger in magnitude than  $U_{k-}/U_j$ .

The relative amplitude of a signal downstream with respect to the reference at  $x/h = 0$  is also calculated with Eq. (4.9) from the first SPOD mode at the screech fundamental frequency. Results are shown in Figure 10(g,h,i) for the external acoustic waves, internal  $k_-$  waves, and internal  $k_+$  waves, respectively. The amplitude of the external acoustic waves does not vary significantly with respect to the reference at  $x/h = 0$ ; on the other hand, both  $k_-$  and  $k_+$  waves grow significantly downstream. The  $k_-$  wave undergoes a series of modulations until reaching a maximum value of  $\alpha \approx 13$ , followed by a rapid decay farther downstream. The  $k_+$  wave grows more smoothly and becomes almost 70 times stronger than the reference at  $x/h = 0$ . Moreover, the  $k_+$  wave has a peak location farther downstream than the  $k_-$  wave and a slower decay rate after the peak.

In order to establish resonance at the screech frequency, the disturbance components

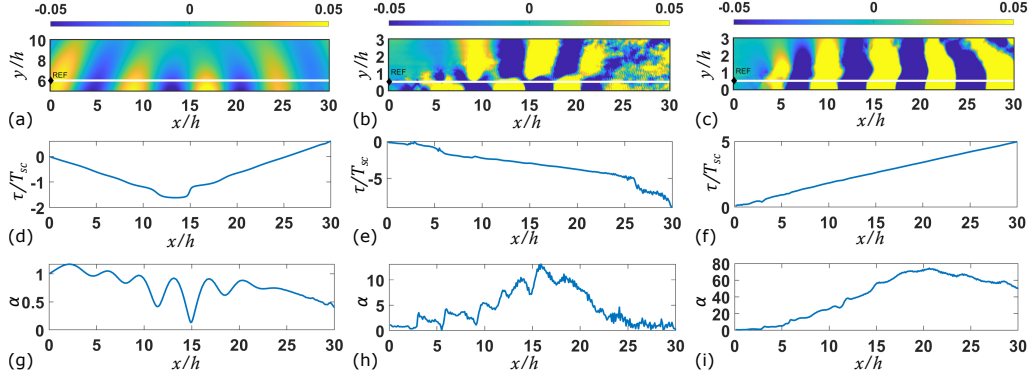


FIGURE 10. (a,b,c) Locations where cross correlation is computed shown by the solid line on top of the SPOD mode, and the reference point is marked by the solid diamond. (d,e,f) Time lag for the external acoustic, internal  $k_-$ , and internal  $k_+$  waves, respectively. (g,h,i) Relative amplitude variation for the external acoustic, internal  $k_-$ , and internal  $k_+$  waves, respectively. Screech case:  $M_j = 1.69$ .

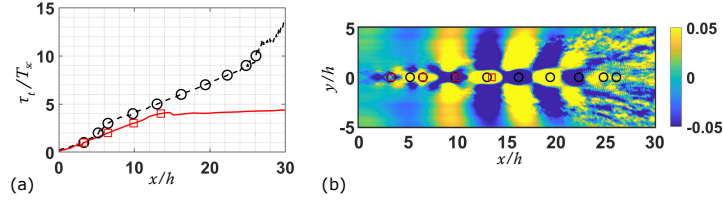


FIGURE 11. (a) Time for the disturbances to complete one feedback loop between the nozzle exit and a point at  $x/h$ . The dashed line indicates an internal feedback path; the solid line indicates an external feedback path, and circles and squares are the identified points of return for the feedback path considered. (b) Overlaying identified points of return on the first  $v'$  SPOD mode with only the upstream component.

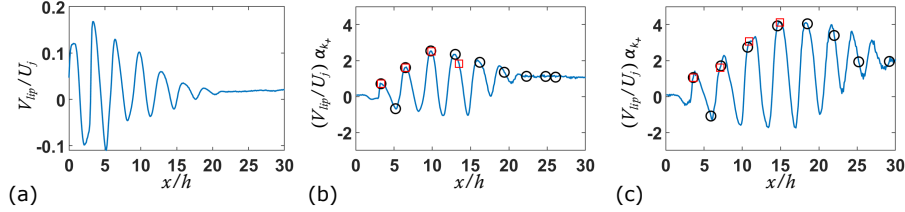


FIGURE 12. (a) Time-averaged transverse velocity  $V_{ip}/U_j$  along the minor lip line for  $M_j = 1.69$ . (b)  $(V_{ip}/U_j)\alpha_{k_+}$  for  $M_j = 1.69$ . (c)  $(V_{ip}/U_j)\alpha_{k_+}$  for  $M_j = 1.78$ .

involved in the feedback loop must satisfy a constructive phase relationship. We define a streamwise location as an eligible point of return for the feedback loop in the following way,

$$x \text{ s.t. : } [\tau_{k_+}(x) - \tau_-(x)]/T_{sc} = \tau_t(x)/T_{sc} = N, \quad (4.10)$$

where  $\tau_-$  is the negative time delay for the upstream closure and can be either  $\tau_{k_-}$  or  $\tau_{c_-}$  depending on the feedback path,  $\tau_t$  is the total time delay for completing one feedback loop,  $T_{sc}$  is the screech period, and  $N$  is a positive integer. The name is chosen to indicate that an upstream-traveling wave disturbance from such a point back to the receptivity

---

$M_j$	$U_j/c_\infty$	$x_s/h$	$U_{c-}/c_\infty$	$U_{c+}/c_\infty$	$\beta_-(\text{deg})$	$\beta_+(\text{deg})$	$U_{k+}/U_j$	$U_{k-}/U_j$
1.56	1.28	11.8	-1.06	1.07	18.8	159	0.62	-0.55
1.69	1.35	13.2	-1.16	1.12	30.6	153	0.65	-0.56
1.78	1.39	15.0	-1.15	1.18	29.1	148	0.67	-0.54

---

TABLE 2. Estimates of the effective source location  $x_s$ , streamwise velocities of the acoustic waves ( $U_{c-}$ ,  $U_{c+}$ ), radiation angles ( $\beta_-$ ,  $\beta_+$ ), and velocities of the internal waves ( $U_{k-}$ ,  $U_{k+}$ ).  $\beta_\pm$  are defined with respect to  $x_s$  measured from the jet axis starting from the inlet direction.

location will be perfectly in phase to sustain the resonance. Using the calculated time delay shown in Figure 10(d,e,f), and assuming the receptivity location is at the nozzle exit  $x/h = 0$ , two sets of points of return, one for the external feedback path and the other for the internal feedback path, are identified and shown in Figure 11(a). To correlate these locations with the coherence structures of the flow field, the points of return are also plotted in Figure 11(b) on top of the first  $v'$  SPOD mode containing only the upstream component. It can be seen that three identified points of return between  $x/h = 6$  and  $x/h = 14$  have closely synchronized feedback paths. In particular, the last of the three, around  $x/h = 13.3$ , coincides with the effective acoustic source location. Interestingly, this point does not correspond to a local maximum of the internal  $k_-$  wave of  $v'$  in the first SPOD mode. Beyond  $x/h = 14$ , there are additional points of return for the internal feedback path where the magnitudes of both  $k_-$  and  $k_+$  waves continue to grow.

Considering the production mechanism of the acoustic waves, one would expect some of the identified points of return to correlate with locations in the flow where the combined interactions of shock and K-H waves are of high amplitude. To check this hypothesis, the product of normalized mean transverse velocity  $V_{lip}/U_j$  and  $\alpha_{k_+}$  measured along the minor lip line is used as a proxy for the strength of shock-instability wave interactions. Figure 12(a) shows the time-averaged oscillations of the flow induced by the shock cells in the jet supersonic core for the case at  $M_j = 1.69$ . The product of  $V_{lip}/U_j$  and  $\alpha_{k_+}$  is obtained for two stronger screech cases at  $M_j = 1.69$  and  $M_j = 1.78$ , and values are shown in Figure 12(b,c), respectively. For both cases, the previously identified effective acoustic source location coincides with the last shared point of return between the two feedback paths and resides almost exactly on the peak of  $(V_{lip}/U_j)\alpha_{k_+}$ .

## 5. Conclusions

Experimentally validated high-fidelity LES of rectangular jet screech are used to study the coherent structures and the acoustic and instability waves associated with screech generation. The leading SPOD modes at the screech fundamental and first harmonic frequencies are extracted from pressure and transverse velocity fluctuations in the jet minor-axis plane, revealing both the coherent structures inside the jet plume and the acoustic waves outside the jet. At the screech frequency, the standing wave patterns from the pressure and velocity SPOD modes are observed; the acoustic waves are seen to originate from spatially distributed phased sources near the end of the supersonic region of the jet plume. Evidence from both the SPOD modes and the FW-H acoustic predictions shows the fundamental screech tone propagates dominantly in specific upstream and downstream angles and the first harmonic tone exhibits multiband patterns

with peak emission at 90 deg due to interference among phased acoustic sources. Spatial cross correlation of the SPOD data is used to determine the effective source locations of the screech acoustic waves, and the streamwise signal propagation velocities for the K-H wave and internal upstream-propagating mode are estimated. For the three screech cases considered, the values are very similar when normalized by the fully expanded jet velocity  $U_j$ : between 0.62 and 0.67 for the K-H wave and between 0.54 and 0.56 for the internal mode. Lastly, using the resonance phase condition, the possible locations downstream of the nozzle where upstream-propagating disturbances can arrive in phase for screech re-excitation at the nozzle exit are determined and compared with the coherent structures in the dominant SPOD mode. For the two possible screech feedback paths, the current analysis does not favor or discriminate either of them as the closure mechanism, and further exploration is warranted in the future.

### Acknowledgments

This work is supported by the Office of Naval Research under grant N00014-18-1-2391 with Dr. Steve Martens as the project manager. We would like to thank Cascade Technologies for their LES solver and Dr. Guillaume A. Brès for his substantial support and guidance on our work. We thank Professor Rajan Kumar from Florida State University for sharing with us the experimental data. We appreciate helpful comments from Dr. Michael Karp on a draft of this work. The computational resources are provided by the XSEDE (TG-CTS190021) program.

### REFERENCES

- ALKISLAR, M. B., KROTHAPALLI, A., & LOURENCO, L. M. 2003 Structure of a screeching rectangular jet: a stereoscopic particle image velocimetry study. *J. Fluid Mech.* **489**, 121–154.
- BOGEY, C. & GOJON, R. 2017 Feedback loop and upwind-propagating waves in ideally expanded supersonic impinging round jets. *J. Fluid Mech.* **823**, 562–591.
- BRÈS, G. A., BOSE, S. T., EMORY, M., HAM, F. E., SCHMIDT, O. T., RIGAS, G., & COLONIUS, T. 2018 Large-eddy simulations of co-annular turbulent jet using a Voronoi-based mesh generation framework. *AIAA Paper* 2018-3302.
- BRÈS, G. A., HAM, F. E., NICHOLS, J. W., & LELE, S.K. 2017 Unstructured large-eddy simulations of supersonic jets. *AIAA J.* **55**, 1164–1184.
- BRÈS, G. A., TOWNE, A., & LELE, S. K. 2019 Investigating the effects of temperature non-uniformity on supersonic jet noise with large-eddy simulation. *AIAA Paper* 2019-2730.
- CHANDRASHEKAR, P. 2013 Kinetic energy preserving and entropy stable finite volume schemes for compressible Euler and Navier-Stokes equations. *Commun. Comput. Phys.* **14**, 1252–1286.
- EDGINGTON-MITCHELL, G. 2019 Aeroacoustic resonance and self-excitation in screeching and impinging supersonic jets – a review. *Int. J. Aeroacoust.* **18**, 118–188.
- EDGINGTON-MITCHELL, D., JAUNET, V., JORDAN, P., TOWNE, A., SORIA, J., & HONNERY, D. 2018 Upstream-travelling acoustic jet modes as a closure mechanism for screech. *J. Fluid Mech.* **855**, R1.
- FFOWCS-WILLIAMS, J. E. & HAWKINGS, D. L. 1969 Sound generation by turbulence and surfaces in arbitrary motion. *Philos. Trans. R. Soc. A* **264**, 321–342.

- FISHER, T. C., & CARPENTER, M. H. 2013 High-order entropy stable finite difference schemes for nonlinear conservation laws: finite domains. *J. Comput. Phys.* **252**, 518–557.
- GOJON, R., BOGEY, C., & MARSDEN, O. 2016 Investigation of tone generation in ideally expanded supersonic planar impinging jets using large-eddy simulation. *J. Fluid Mech.* **808**, 90–115.
- GOJON, R., GUTMARK, E., & MIHAESCU, M. 2019 Antisymmetric oscillation modes in rectangular screeching jets. *AIAA J.* **57**, 3422–3441.
- LOCKARD, D. P. 2000 An efficient two-dimensional implementation of the Ffowcs-Williams and Hawkins equation. *J. Sound Vib.* **229**, 897–911.
- LUMLEY, J. L. 1970 *Stochastic Tools in Turbulence*. Academic Press.
- MAJUMDAR, D. 2014 America’s \$400 billion stealth jet fleet is grounded. Apr.14, *The Daily Beast News*
- NEKKANTI, A., & SCHMIDT, O. T. 2020 Modal analysis of the directivity of acoustic emissions from wavepackets in turbulent jets. *AIAA Paper* 2020-0745.
- PANDA, J. 1999 An experimental investigation of screech noise generation. *J. Fluid Mech.* **378**, 71–96.
- POWELL, A. 1953 On the mechanism of choked jet noise. *Proc. Phys. Soc.* **66**, 1039–1056.
- RAMAN, G. 1997 Screech tones from rectangular jets with spanwise oblique shock-cell structures. *J. Fluid Mech.* **330**, 141–168.
- RAMAN, G. 1999 Supersonic jet screech: half-century from Powell to the present. *J. Sound Vib.* **225**, 543–571.
- RAMAN, G., PANICKAR, P., & CHELLIAH, K. 2012 Aeroacoustics of twin supersonic jets: a review. *Int. J. Aeroacoust.* **11**, 957–984.
- SCHMIDT, O. T., & COLONIUS, T. 2020 Guide to spectral proper orthogonal decomposition. *AIAA J.* **58**, 1023–1033.
- SCHMIDT, O. T., TOWNE, A., RIGAS, G., COLONIUS, T., & BRÈS, G. A. 2018 Spectral analysis of jet turbulence. *J. Fluid Mech.* **855**, 953–982.
- TADMOR, E. 2003 Entropy stability theory for different approximations of nonlinear conservation laws and related time-dependent problems. *Acta Numer.* **12**, 451–512.
- TAM, C. K. W., SEINER, J. M., & YU, J. C. 1986 Proposed relationship between broadband shock associated noise and screech tones. *J. Sound Vib.* **110**, 309–321.
- TAM, C. K. W. & AHUJA, K. K. 1990 Theoretical model of discrete tone generation by impinging jets. *J. Fluid Mech.* **214**, 67–87.
- TAM, C. K. W. & HU, F. Q. 1989 On the three families of instability waves of high-speed jets. *J. Fluid Mech.* **201**, 447–483.
- TOWNE, A., SCHMIDT, O. T., & COLONIUS, T. 2018 Spectral proper orthogonal decomposition and its relationship to dynamic mode decomposition and resolvent analysis. *J. Fluid Mech.* **847**, 821–867.
- VALENTICH, G., UPADHYAY, P., & KUMAR, R. 2016 Mixing characteristics of a moderate aspect ratio screeching supersonic rectangular jet. *Exp. Fluids* **57**, 71–84.
- WU, G. J., LELE, S. K., & JEUN, J. 2020a Numerical study of screech produced by a rectangular supersonic jet. *AIAA Paper* 2020-2559.
- WU, G. J., LELE, S. K., JEUN, J., KUMAR, R., & GUSTAVSSON, J. 2020b Unstructured large-eddy simulations of rectangular jet screech: assessment and validation. *AIAA J.* (To appear).